Mineralogical Magazine (2020), **84**, 398–411
doi:10.1180/mgm.2020.29

CAMBRIDGE UNIVERSITY PRESS

Article

Texture and composition of magnetite in the Duotoushan deposit, NW China: implications for ore genesis of Fe–Cu deposits

Xia Hu[1,2,3], Huayong Chen[1,4*], Xiaowen Huang[5] and Weifeng Zhang[6]

[1]Key Laboratory of Mineralogy and Metallogeny, Guangzhou Institute of Geochemistry, Chinese Academy of Sciences, Guangzhou 510640, China; [2]University of Chinese Academy of Sciences, Beijing 100049, China; [3]Département de Géologie et de Génie Géologique, Université Laval, Québec, QC G1V 0A6, Canada; [4]Guangdong Provincial Key Laboratory of Mineral Physics and Materials, Guangzhou 510640, China; [5]State Key Laboratory of Ore Deposit Geochemistry, Institute of Geochemistry, Chinese Academy of Sciences, Guiyang 550081, China; and [6]Wuhan Center of China Geological Survey, Wuhan 430205, China

Abstract

The Duotoushan deposit is an important Fe–Cu deposit in the Aqishan–Yamansu metallogenic belt of eastern Tianshan, NW China. Magnetite occurs in two main habits which are common in many Fe–Cu deposits, i.e. platy (T_{D1} Mag) and granular magnetite (T_{D2} Mag) have been identified at Duotoushan. Platy magnetite shows two different zones (bright and dark) based on the observations by scanning electron microscopy. The bright part (T_{D1}-L) is the main part of T_{D1} magnetite and lacks inclusions. The dark part (T_{D1}-D) is very porous and has abundant tiny silicate inclusions. Granular magnetite is usually anhedral with obvious oscillatory zoning in back-scattered electron images. In general, the dark zones of magnetite are characterised by greater Si, Ca, Al and lesser Fe contents than the bright zones. *In situ* X-ray diffraction (XRD) analysis shows that the lattice parameter of T_{D1} magnetite is approximately equal to that of standard magnetite and slightly higher than that of T_{D2} magnetite, indicating that some cations with ionic radii smaller than those of Fe^{2+} or Fe^{3+} entered the magnetite lattice by simple or coupled substitution mechanisms in T_{D2} magnetite.

The results in the present study show that the effects of temperature and f_{O_2} on platy magnetite are very limited and the changing fluid composition might be the major controlling factor for the formation of Duotoushan platy magnetite. Although the possibility that mushketovite transformed from hematite cannot be excluded entirely, evidence from *in situ* XRD data, pore-volume ratio calculation and the growth habit of intergrown minerals indicates that platy magnetite (T_{D1}) coexisting with amphibole was more likely to have been precipitated originally from hydrothermal fluid. This was then affected by changes in the fluid composition which consequently led to dissolution of primary magnetite (T_{D1}-L) and re-precipitation of T_{D1}-D magnetite (with abundant porosity and mineral inclusions). Meanwhile, granular magnetite (T_{D2}) with oscillatory zoning, and coexisting with epidote and quartz, was precipitated from fluid with periodic variation in temperature. These oscillatory zones are characterised by bands enriched in Si, Al and Ca alternating with bands depleted in these elements. The present investigation revealed a complex evolutionary process for magnetite formation in the Duotoushan deposit. The importance of combined investigation of texture and compositional characterisation of magnetite for study of the ore genesis and evolution of Fe–Cu deposits is highlighted.

Keywords: Magnetite, Fe–Cu deposit, texture and mineral composition, ore genesis, NW China

(Received 23 December 2019; accepted 23 April 2020; Accepted Manuscript published online: 27 April 2020;
Associate Editor: Andrew G. Christy)

Introduction

Magnetite is a common mineral in various Fe–Cu deposits, which contain a variety of minor and trace elements such as Al, Si, Ca, Mg, Mn, Ti, V, Cr and Ni. The composition of magnetite has been used widely as a petrogenetic indicator (Dare *et al.*, 2014; Nadoll *et al.*, 2014) and to discriminate various deposit types or ore-forming processes (Carew 2004; Singoyi *et al.*, 2006; Rusk *et al.*, 2009; Dupuis and Beaudoin, 2011; Dare *et al.*, 2012; Nadoll *et al.*, 2012; Knipping *et al.*, 2015a,b; Huang *et al.*, 2015a,b, 2016; Hu *et al.*, 2017; Alaminia *et al.*, 2020). Recent studies (e.g. Hu *et al.*, 2014, 2015; Wen *et al.*, 2017; Yin *et al.*, 2017; Huang *et al.*, 2018; Hu *et al.*, 2020) have shown that combined textural and compositional studies are necessary before using these magnetite data for provenance and petrogenetic purposes.

Magnetite in Fe–Cu deposits usually has two crystal habits, i.e. platy and granular (Huang *et al.*, 2014; Apukhtina *et al.*, 2017). Platy magnetite is commonly considered to be 'mushketovite', i.e. formed by replacement of hematite. Previous studies usually considered platy and granular magnetite as the same type and used their compositional data to discuss their genesis and distinguish different deposit types (Günther *et al.*, 2017; Felipe *et al.*, 2014). However, whether the same mechanism is responsible for these two types of magnetite remains unknown.

The Duotoushan deposit is an important Fe–Cu deposit in the Aqishan–Yamansu metallogenic belt of eastern Tianshan, NW China. A number of studies has been carried out since its discovery in the 1970s. The genesis of this deposit remains controversial. Jia and Zhao (2017) suggested that the Duotoushan deposit is a

*Author for correspondence: Huayong Chen, Email: huayongchen@gig.ac.cn
Cite this article: Hu X., Chen H., Huang X. and Zhang W. (2020) Texture and composition of magnetite in the Duotoushan deposit, NW China: implications for ore genesis of Fe–Cu deposits. *Mineralogical Magazine* **84**, 398–411. https://doi.org/10.1180/mgm.2020.29

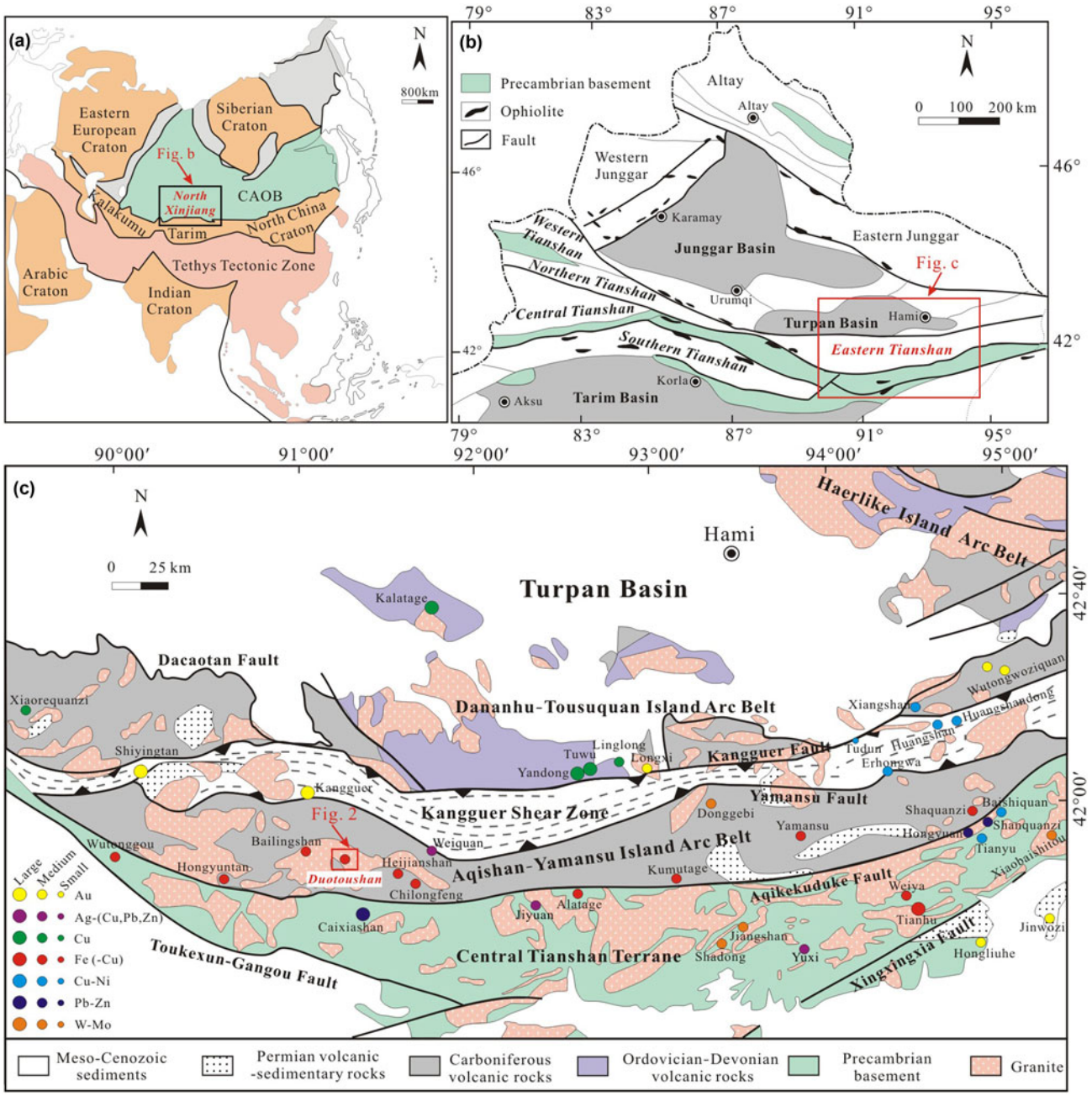

Fig. 1. Geological map showing the main units in the Eastern Tianshan area and location of the Duotoushan Fe–Cu deposit in the Tugutublak Formation. (*a*) Location of the Central Asian Orogenic belt (CAOB). (*b*) Location of Eastern Tianshan. (*c*) Location and major tectonic units in Eastern Tianshan. (Fig. 1a modified after Sengör and Natal'in (1996); Fig. 1b simplified after Chen *et al.* (2012); Fig. 1c modified after Wang *et al.* (2006) and Deng *et al.* (2014).)

medium–high-temperature hydrothermal magnetite deposit characterised by fracture infill, while Zhang *et al.* (2018) concluded, based on the mineralogy, paragenesis and fluid-inclusion studies, that it is similar to the Central Andean iron oxide–copper–gold (IOCG) deposits. Both platy and granular magnetite are common and constitute the major orebody at Duotoushan (Zhang *et al.*, 2018).

In the present investigation, textural and compositional data of two types of magnetite from the Duotoushan deposit are presented. The data are used to discuss the factors controlling the magnetite composition and the links between this and the texture. The origins of the two magnetite types and implications for genesis of the Duotoushan and other similar Fe–Cu deposits are discussed.

District and deposit geology

Eastern Tianshan, located between the Tarim and Junggar blocks in north Xinjiang, is an important part of the Central Asian Orogenic Belt (Fig. 1*a*,*b*). The Central Asian Orogenic Belt is a tectonic collage of ophiolite suites, magmatic arc remnants, Precambrian massifs and accretionary terranes (Windley *et al.*, 1990; Sengör *et al.*, 1993; Sengör and Natal'in, 1996) formed from the Carboniferous to Early Triassic collisions among the Siberia and Tarim–Sino–Korean plates along

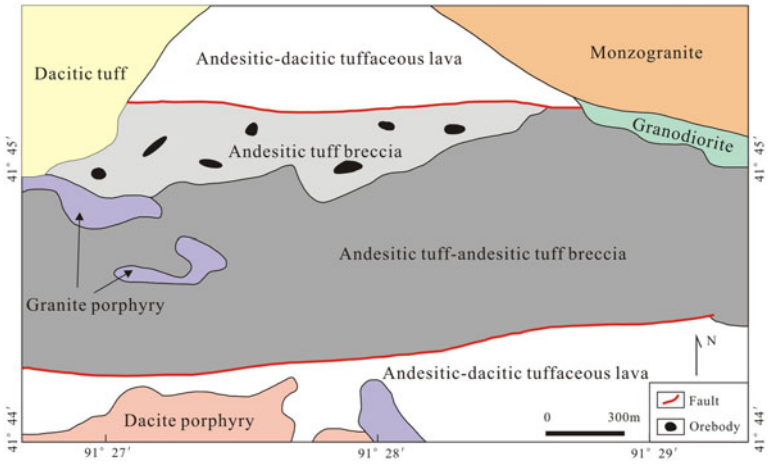

Fig. 2. Geological map of the Duotoushan Fe–Cu deposit (modified from Sang *et al.*, 2003).

the Solonker suture (Chen *et al.*, 2007, 2009, 2012; Xiao *et al.*, 2010). Eastern Tianshan is divided into the Dananhu–Tousuquan Island Arc Belt, the Kangguer Shear Zone, the Aqishan–Yamansu Island Arc Belt and the Central Tianshan Terrane (from north to south) by nearly E–W-trending faults (Fig. 1c). The Aqishan–Yamansu Island Arc Belt is considered to be one of the most important Fe (–Cu) belts in NW China and hosts numerous high-grade Fe deposits (>45% total Fe), e.g. the Hongyuntan, Bailingshan, Duotoushan and Shaquanzi deposits (Wang *et al.*, 2005, 2006; Zhang *et al.*, 2012; Huang *et al.*, 2013; Hou *et al.*, 2014).

The stratigraphy in the Duotoushan Fe–Cu deposit consists of the Upper Carboniferous Tugutublak Formation composed principally of andesitic–dacitic lava/breccias (Fig. 2). The Tugutublak volcanic–sedimentary rocks were intruded by granodiorite, granite porphyry, monzogranite, and dacite porphyry. These are predominantly located in the eastern-, western- and southwestern parts of the Duotoushan deposit. There are at least two sub-parallel faults (E–W-trending) in this deposit (Sang *et al.*, 2003; Fig. 2).

The ore bodies of the Duotoushan Fe–Cu deposit are mostly stratabound and mainly hosted in the andesitic tuff breccias. Previous exploration reported seven stratabound bodies in the deposit. These ore bodies are 50–248 m long and 4–70 m wide, with average ore grade of 45 wt.% Fe. The copper grade in some ore bodies can be up to 0.7–1.0 wt.% (Sang *et al.*, 2003). According to the Xinjiang Bureau of Geology and Mineral Resources, the Duotoushan is classified as a medium-sized Fe deposit (usually >0.1 Mt in China), although no ore reserve data have been published (Sang *et al.*, 2003).

Five stages of alteration and mineralisation were identified at Duotoushan based on detailed petrological studies, including: (I) albite–amphibole stage; (II) garnet–clinopyroxene stage; (III) magnetite mineralisation stage; (IV) sulfide stage; and (V) late veins stage (Zhang *et al.*, 2018). The albite–amphibole stage contains abundant albite and minor amphibole. The coarse pink albite and dark-grey amphibole are usually crosscut by magnetite (Zhang *et al.*, 2018). The garnet–clinopyroxene stage contains major light brown to yellowish-green garnet with minor clinopyroxene, which were partially or entirely replaced by amphibole, epidote and magnetite (Zhang *et al.*, 2018). Stage III is the main stage associated with magnetite at Duotoushan. This stage can be divided into two sub-stages of different mineral assemblages (stage III-A and stage III-B) and correspond to two different types of magnetite. One is platy magnetite in stage III-A which coexists with amphibole, pyrite and chalcopyrite (Fig. 3a). Platy magnetite is commonly intergrown with amphibole replaced by quartz (Fig. 3b), which may indicate broadly coeval formation. Another is euhedral granular magnetite in stage III-B which coexists with epidote, quartz, amphibole, pyrite and chalcopyrite (Figs. 3c). Granular magnetite usually has a straight boundary with epidote and quartz, indicating simultaneous formation (Figs. 3d). The minerals in the sulfide stage are mainly pyrite and chalcopyrite. Pyrite-rich veins crosscutting stage-III magnetite suggest that the sulfide stage is later than the magnetite stage (Zhang *et al.*, 2018). The late-veins stage consist of mainly quartz and calcite veins which cross-cut early-stage minerals.

Sampling and analytical methods

Representative samples of two different types of magnetite from stage III were selected for the investigation.

Polished thin sections were carbon-coated and then investigated using a ΣIGMA scanning electron microscope (SEM) in back-scattered electron (BSE) mode at the Sun Yat-sen University, Guangzhou, China. The *in situ* micro-XRD analyses were conducted using a Rigaku D/max Rapis IIR micro-XRD system at the Central South University, Changsha, China. All analyses were carried out at 40 kV and 250 mA (CuKα) with exposure times of 22 min. The X-ray beam was ~40 μm in diameter and was focused on the selected spots on the thin sections. The compositions of magnetite were analysed using a JEOL JXA-8230 electron probe micro-analyser (EPMA) at Southwest Petroleum University. The analyses were carried out at 15 kV, 20 nA beam current and 1 μm spot size. Peak counting times ranged from 20 s to 60 s for various elements. The standards used were: magnetite (Fe); almandine garnet (Si,Mg); diopside (Ca); pyrope garnet (Al); rhodonite (Mn); Ni metal; V metal; rutile (Ti); and synthetic Cr_2O_3 (Cr). In addition, zoning in magnetite grains was mapped for Fe, Si, Ca and Al, using an accelerating voltage of 20 kV, a probe current of 300 nA, and a beam size of 2 μm. Fe was analysed using a LIF crystal. Si and Al were analysed using a TAP crystal. Ca was analysed using a PET crystal. The dwell time for each point was 100 ms.

Results

Morphology and texture of magnetite

Magnetite in the Duotoushan deposit can be classified into platy (T_{D1} Mag) and granular (T_{D2} Mag) types. The T_{D1} magnetite is

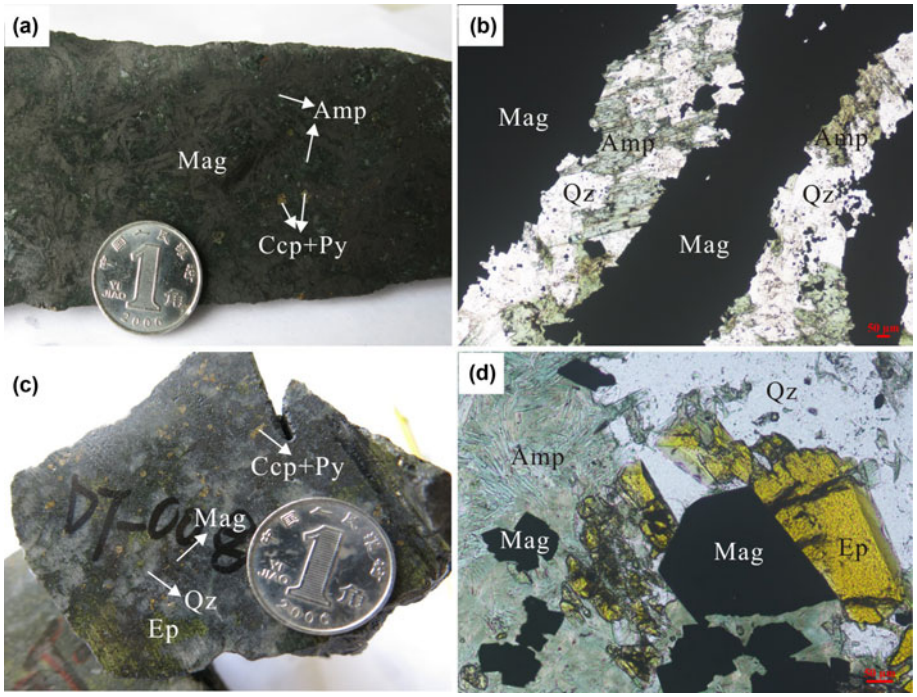

Fig. 3. Photographs of magnetite from the Duotoushan deposit. (*a*) Platy magnetite ore, contains mainly magnetite, amphibole and a small amount of pyrite and chalcopyrite; (*b*) platy magnetite intergrown with amphibole; amphibole is replaced by quartz; (*c*) granular magnetite ore, contains mainly epidote, quartz, pyrite and chalcopyrite; (*d*) granular magnetite closely associated with epidote and quartz. Mineral abbreviations (from Whitney and Evans, 2010): Mag: magnetite, Amp: amphibole, Qz: quartz, Ccp: chalcopyrite, Py: Pyrite, Ep: epidote.

commonly intergrown with amphibole (Figs 3b, 4a). It shows two different zones (bright and dark) based on observation by SEM (Fig. 4b). The bright zone (T_{D1}-L Mag) is the main part of the T_{D1} magnetite and is free of inclusions, whereas the dark part (T_{D1}-D Mag) contains abundant porosity and tiny silicate inclusions (Fig. 4c–e). The T_{D2} magnetite usually coexists with epidote, quartz and amphibole and was replaced locally by hematite (Figs 3d, 4f). It is commonly euhedral with obvious oscillatory zoning in the BSE images (Fig. 4g).

XRD patterns of magnetite

The XRD data for Duotoushan magnetite are presented in the Supplementary Data Table A1. The XRD pattern of the T_{D1} magnetite has a cell parameter of $a = 8.397(1)$ Å, identical to the standard magnetite (*PDF No. 19-0629, $a = 8.396$ Å). The strong intensity, small cell parameter, together with the sharp 2θ of the {311} peak of full-width at half maximum (FWHM) of 0.188° (Fig. 5) indicate that it is well crystallised. The cell parameter of the T_{D2} magnetite is $a = 8.383(4)$ Å, which is less than both the T_{D1} magnetite and the standard magnetite. The intensity and the 2θ of {311} peak (FWHM = 0.185°) is similar to that of the T_{D1} magnetite (Fig. 5).

Composition of magnetite

Electron microprobe analysis elemental mapping provided information on major- and trace-element distribution patterns within individual T_{D1} and T_{D2} magnetite crystals from the Duotoushan deposit (Fig. 6). The dark zones of T_{D1} magnetite are characterised by larger amounts of Si, Ca, Al and smaller Fe contents than the bright zones (Fig. 6a). The T_{D2} magnetite displays similar variations to that of the T_{D1} magnetite in which the dark domain of magnetite contains more Si, Ca, Al and less Fe than the bright domain (Fig. 6b).

Representative compositions of the Duotoushan magnetite are presented in Table 1 (extensive data are presented in Supplementary Data Table A2). The platy magnetite from the Duotoushan Fe–Cu deposit forms two compositional groups, corresponding to the bright (T_{D1}-L magnetite) and dark (T_{D1}-D magnetite) domains (Fig. 7). The T_{D1}-L magnetite contains less SiO_2 (0.113–0.306 wt.%), CaO (below the detection limits), MgO (0.01–0.024 wt.%), Al_2O_3 (0.035–0.052 wt.%), Cr_2O_3 (<0.01–0.021 wt.%) and more total-FeO (92.268–93.433 wt.%), whereas the T_{D1}-D magnetite contains significantly more SiO_2 (2.267–3.433 wt.%), CaO (0.222–0.648 wt.%), MgO (0.011–0.288 wt.%,), Al_2O_3 (0.096–0.338 wt.%), Cr_2O_3 (0.015–0.032 wt.%) and less total-FeO (88.518–91.011 wt.%). In addition, The T_{D1}-L magnetite has contains similar amounts of MnO (0.036–0.069 wt.%) and slightly less TiO_2 (<0.01–0.025 wt.%) than T_{D1}-D magnetite (0.044–0.076 wt.%, <0.01–0.03 wt.%, respectively). Most of the V_2O_3 and NiO contents of the platy magnetite are below the detection limits.

The granular magnetite also contains two compositional groups (Fig. 7). The T_{D2}-L magnetite contains less SiO_2 (0.158–1.249 wt.%), CaO (below the detection limit), MgO (<0.01–0.035 wt.%), Al_2O_3 (<0.017–0.253 wt.%, average: 0.064 wt.%), MnO (0.027–0.094 wt.%), TiO_2 (<0.01–0.042 wt.%) and more total FeO (91.547–93.314 wt.%), than T_{D2}-D magnetite which contains more SiO_2 (0.984–3.207 wt.%), CaO (0.03–0.644 wt.%), MgO (0.018–0.137 wt.%), Al_2O_3 (0.221–0.714 wt.%), MnO (0.049–0.135 wt.%), TiO_2 (<0.014–0.175 wt.%) and less total-FeO (87.860–91.358 wt.%). The T_{D2}-L magnetite contains similar amounts of Cr_2O_3 (<0.01–0.032 wt.%) and V_2O_3 (<0.01–0.023 wt.%) to T_{D2}-D magnetite (<0.01–0.044 wt.%, <0.01–0.025 wt.%, respectively). The NiO contents of the granular magnetite are mostly below the detection limit.

*Powder diffraction files from the International Centre for Diffraction Data, http://www.icdd.com/

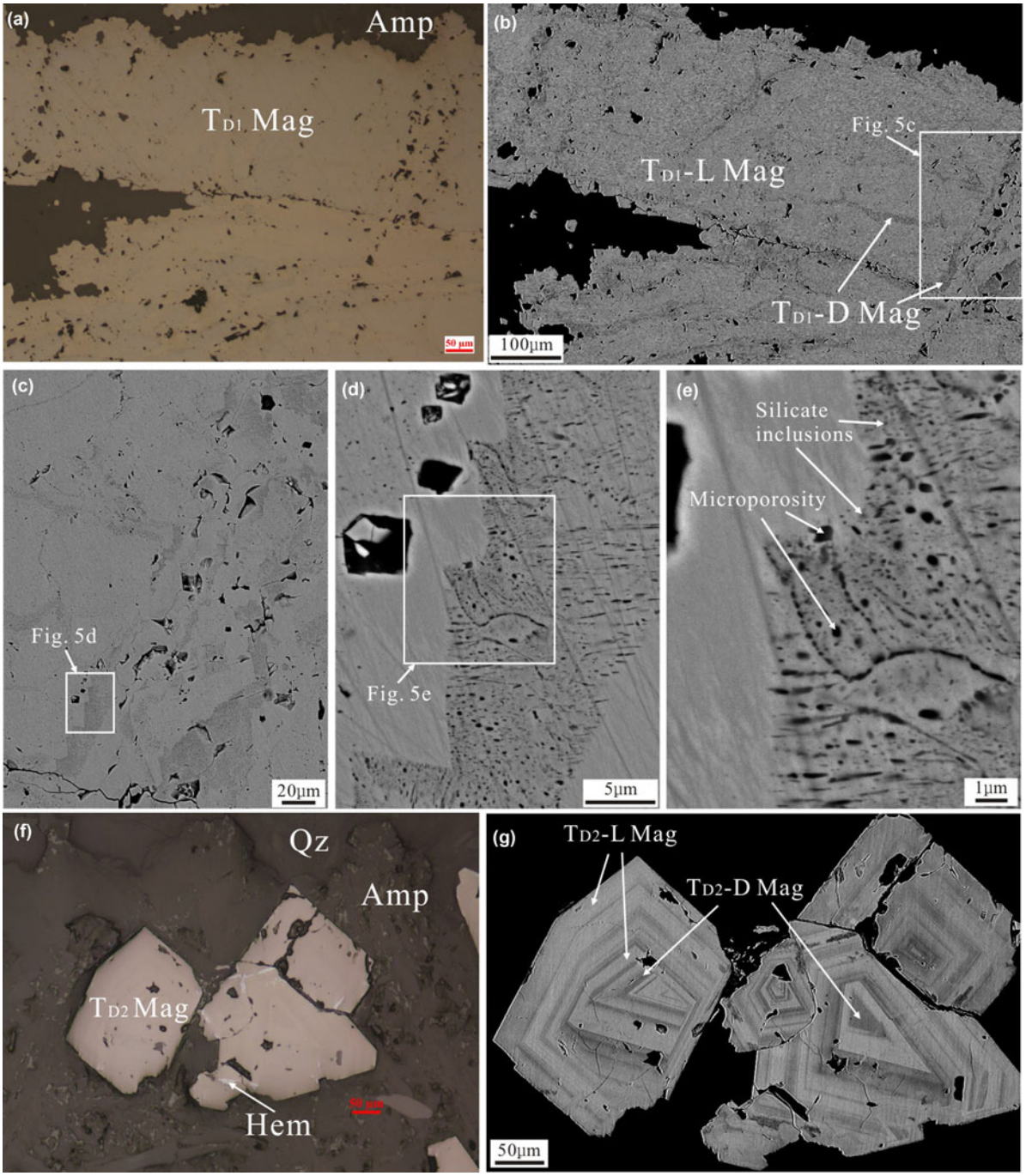

Fig. 4. Photomicrographs (*a*, *f*) and BSE images (*b*–*e*, *g*) of the Duotoushan magnetite. (*a*) Photomicrograph of platy magnetite (T_{D1} Mag). (*b*–*e*) BSE images of platy magnetite, which shows different zones. The T_{D1}-L magnetite is the bright domain. The T_{D1}-D magnetite is the dark domain with abundant microporosity and silicate inclusions. (*f*) Photomicrograph of granular magnetite (T_{D2} Mag). (*g*) BSE image of platy magnetite, which shows obvious oscillatory zones. Mineral abbreviations (from Whitney and Evans, 2010): Mag: magnetite, Amp: amphibole; Qz: quartz; Hem: hematite.

Discussion

Element-substitution mechanisms for magnetite

Magnetite has an inverse spinel structure with the formula $Fe^{2+}Fe^{3+}_2O_4$, where tetrahedral sites are occupied exclusively by Fe^{3+} and octahedral sites are occupied randomly by unequal numbers of Fe^{3+} and Fe^{2+} (Lindsley, 1976; Wechsler *et al.*, 1984; Nadoll *et al.*, 2014). Nadoll *et al.* (2014) concluded that divalent cations such as Ca^{2+}, Mg^{2+}, Mn^{2+}, Zn^{2+} and Ni^{2+} can enter into the magnetite lattice by substituting for Fe^{2+}, whereas some trivalent cations such as Al^{3+}, V^{3+} and Cr^{3+} enter by replacing Fe^{3+}. In addition, some tetravalent cations, such as Si^{4+} and Ti^{4+}, can also enter into the magnetite structure when substitution is coupled with a divalent cation (Newberry *et al.*, 1982; Wechsler *et al.*, 1984; Westendorp *et al.*, 1991; Xu *et al.*, 2014).

In the present investigation, the lattice parameter of the T_{D1} magnetite (8.397 Å) is almost equal to that of the standard magnetite (8.396 Å, Fukasawa *et al.*, 1993), whereas the equivalent value for T_{D2} magnetite (8.383 Å) is significantly less than the standard magnetite. For T_{D2} magnetite (including T_{D2}-L and

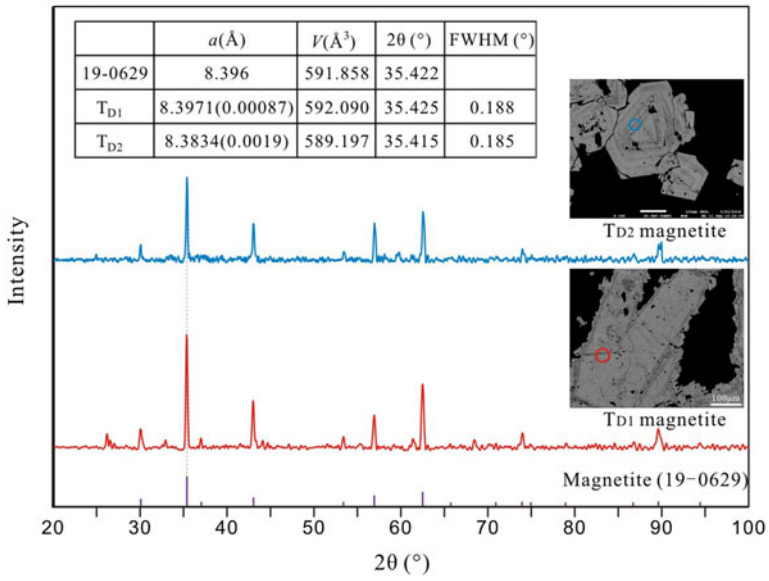

Fig. 5. *In situ* XRD patterns of magnetite from the Duotoushan deposit compared with the standard magnetite (19-0629). The circles are 40 μm in diameter and represent the test area.

T_{D2}-D) the negative correlations of Fe^{3+} with Si^{4+}, Fe^{2+}, Al^{3+}, Ca^{2+} (Fig. 8a, c, d, e) and the positive correlation between Fe^{2+} and Si^{4+} (Fig. 8b) might indicate that these elements entered the intracrystalline sites of magnetite by the following substitutions:

$$^{IV}Si^{4+} + \left(Fe^{2+}, Ca^{2+}\right) \rightarrow {}^{IV}Fe^{3+} + Fe^{3+}$$

$$^{IV}Al^{3+} \rightarrow {}^{IV}Fe^{3+}$$

In these substitutions, the smaller ionic radii of $^{IV}Si^{4+}$ and $^{IV}Al^{3+}$ than of $^{IV}Fe^{3+}$ (0.26 Å, 0.39 Å and 0.49 Å, respectively; Shannon, 1976) can result in the lattice parameter of T_{D2} magnetite in Duotoushan being less than that of standard magnetite. The T_{D1}-L magnetite which is the main T_{D1} magnetite, contains the smallest concentrations of these cations and shows no obvious correlations, indicating that little substitution has occurred in the T_{D1} magnetite. In addition, because we haven't made a further observation on a nanoscale, the possibility that these correlations between Fe and other elements may be caused by silicate nanoparticles cannot be precluded.

Compositional zoning in magnetite

At Duotoushan, both the platy and granular magnetites show zoning with different features. In platy magnetite, the T_{D1}-L magnetite is inclusion-poor and has brighter BSE contrast, whereas the darker T_{D1}-D magnetite contains many tiny inclusions (Fig. 4b-e). Granular magnetite exhibits oscillatory zoning composed of bright and dark bands of varying widths (Fig. 4g). These zones are characterised by micrometre-scale bands enriched in Si, Ca and Al alternating with bands depleted in these elements (Fig. 6).

Irregular compositional zones of platy magnetite are very common in some IOCG deposits (e.g. Candelaria deposit; Huang *et al.*, 2019); iron oxide-apatite (IOA) deposits (e.g. Los Colorados, Chadormalu and El Romeral deposits; Knipping *et al.*, 2015a,b; Deditius *et al.*, 2018; Heidarian *et al.*, 2016; Huang and Beaudoin, 2019); Fe skarn deposits (e.g. Chengchao, Yamansu and Paxton deposits; Hu *et al.*, 2014, 2015; Huang *et al.*, 2018); and volcanogenic massive sulfide (VMS) deposits (e.g. Izok Lake and Halfmile Lake deposits; Makvandi *et al.*, 2016). The compositional variations of different generations/types of magnetite are generally interpreted as the results of dissolution and re-precipitation processes (Putnis, 2009; Putnis and John, 2010; Hu *et al.*, 2014, 2015; Heidarian *et al.*, 2016). Primary magnetite (T_{D1}-L) could be replaced extensively by a secondary variety (T_{D1}-D), preferentially along fractures and/or grain boundaries that have abundant porosity (Hu *et al.*, 2015).

The oscillatory zoning of granular magnetite is similar to magnetite from some skarn deposits (e.g. Vegas Peledas and Ocna de Fier-Dognecea deposits; Dare *et al.*, 2014; Ciobanu and Cook, 2004; Tengtie Fe deposit; Zhao and Zhou, 2015), IOCG deposits (e.g. Sossego deposit; Huang and Beaudoin, 2019) and IOA deposits (e.g. Los Colorados and El Laco deposits; Dare *et al.*, 2015; Knipping *et al.*, 2015b; Huang and Beaudoin, 2019). This zoning of magnetite is generally interpreted as growth zoning caused by variations in fluid compositions and/or physicochemical conditions such as temperature and oxygen fugacity) during fast crystal growth, which periodically change trace-element partition between magnetite and fluids (Shimazaki, 1998; Ciobanu and Cook, 2004; Dare *et al.*, 2014; Knipping *et al.*, 2015b; Makvandi *et al.*, 2015; Huang *et al.*, 2018). Consequently, the oscillatory zoning of granular magnetite from the Duotoushan deposit might be derived from a fluctuating fluid composition and/or physicochemical conditions.

Factors controlling the compositions of magnetite

As reviewed by Nadoll *et al.* (2014), the compositions of hydrothermal magnetite might be mostly controlled by factors such as: fluid composition; host rock; precipitation of associated minerals; temperature (T); and oxygen fugacity (f_{O_2}) during mineral formation.

The host rocks of both platy and granular magnetite are andesitic tuff breccias which consist mainly of euhedral–subhedral albite and amphibole (Zhang *et al.*, 2018). Thus, the host-rock

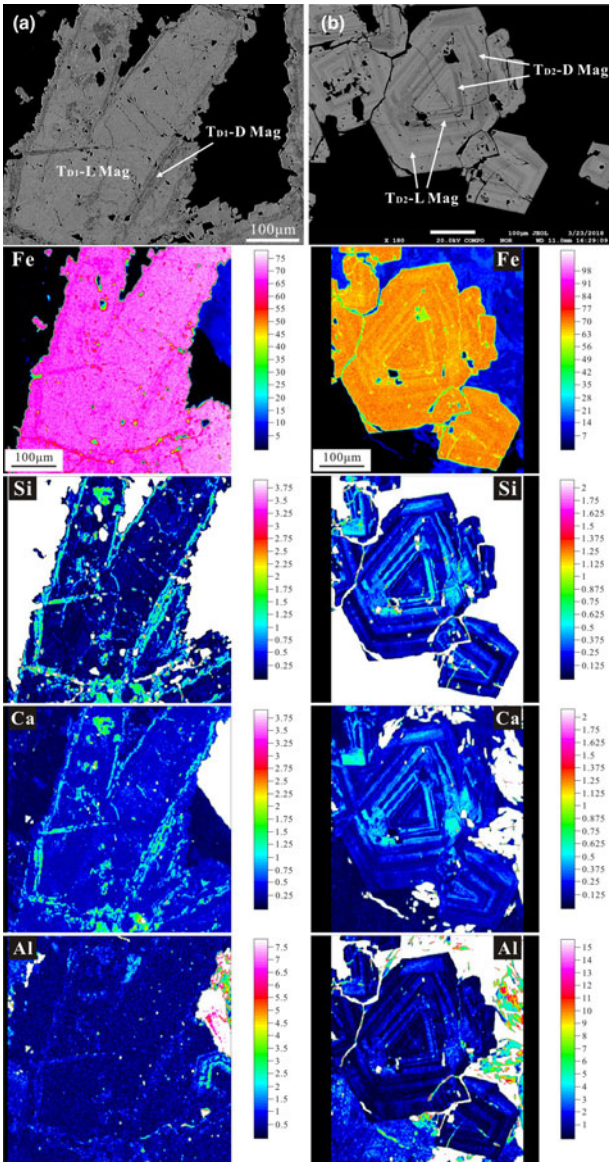

Fig. 6. X-ray compositional mapping of selected elements in different types of magnetite from the Duotoushan deposit: (*a*) platy magnetite; (*b*) granular magnetite; colour scale is in weight percent.

properties might not be the major controlling factors of the highly-variable compositions of these two types of magnetite. Minerals associated with magnetite may affect the contents of some elements within magnetite because of different partition coefficients (Nadoll *et al.*, 2014; Dare *et al.*, 2014; Chen *et al.*, 2015). At Duotoushan, the mineral assemblages of the two types of magnetite are different from each other. T_{D1} magnetite is associated with amphibole which is mainly composed of Si, Mg, Ca and Fe (Zhang *et al.*, 2018). T_{D2} magnetite is mainly associated with epidote, quartz and minor amphibole. The Duotoushan epidote is mainly composed of Si, Fe, Ca and Al (Zhang *et al.*, 2018). It is expected that co-precipitation of amphibole would have decreased the concentration of Mg for incorporation in T_{D1} magnetite and co-precipitation of epidote would have decreased Al for incorporation in T_{D2} magnetite, which suggests that T_{D1} magnetite should contain less Mg and more Al than the T_{D2} magnetite. Interestingly, however, T_{D1}-L magnetite has contents of Mg and Al which are similar to those of T_{D2}-L magnetite and T_{D1}-D magnetite contains significantly more Mg and less Al than T_{D2}-D magnetite. This might indicate that the co-precipitation of amphibole or epidote with these two types of magnetite has no significant effect on its composition.

Temperature is considered to be a major composition-controlling factor for hydrothermal magnetite because element-partition coefficients are very temperature dependent (McIntire, 1963). Titanium and Al in Fe oxides are considered to be positively correlated with temperature, with high-temperature magnetite having high Ti and Al contents (Dare *et al.*, 2012; Nadoll *et al.*, 2012; Canil *et al.*, 2016). For the T_{D1} magnetite at Duotoushan, the T_{D1}-D magnetite has similar Ti and slightly greater Al contents than T_{D1}-L (Fig. 9*a*), indicating that temperature only increases slightly from T_{D1}-L to T_{D1}-D magnetite. For T_{D2} magnetite, the Ti and Al contents of T_{D2}-D magnetite are apparently greater than for T_{D2}-L magnetite, indicating that temperature obviously increased from T_{D2}-L to T_{D2}-D magnetite (Fig. 9*a*).

Oxygen fugacity can also affect the composition of magnetite by controlling element partition coefficients. Some elements, such as V, can occur in various valence states and therefore their behaviours are strongly linked to f_{O_2} (Nielsen *et al.*, 1994; Righter *et al.*, 2006). The oxidation state of V in natural environments varies from + 3 to + 5. Among these species, V^{3+} has the greatest compatibility with the spinel structure of magnetite (e.g. Balan *et al.*, 2006; Righter *et al.*, 2006). Vanadium is incompatible at high oxygen fugacity levels due to its 5+ oxidation state. Therefore, the partition coefficient of magnetite/liquid for V decreases with increasing f_{O_2} because V^{3+} is less stable under these conditions. For Duotoushan magnetite, the mean and median of V contents in T_{D1}-L magnetite are slightly less than those in T_{D1}-D magnetite, indicating that f_{O_2} decreased slightly from T_{D1}-L to T_{D1}-D magnetite (Fig. 9*b*). Because the V contents in T_{D1} magnetite are mostly less than the detection limits, however, the indication of such trends in platy magnetite may be limited. Similarly, the mean and median V contents in T_{D2}-L magnetite are slightly less than those in T_{D2}-D magnetite indicating a slightly decreased f_{O_2} from T_{D2}-L to T_{D2}-D magnetite (Fig. 9*b*). In general, the highly variable compositions of different granular magnetite zones might not be caused by oxygen fugacity.

We can conclude, therefore that the effects of co-precipitating minerals, temperature and f_{O_2} on platy magnetite are very limited and the changing or evolving fluid composition might be the major controlling factor for platy magnetite (especially the late T_{D1}-D) of Duotoushan. According to the paragenesis study and stable-isotope compositions of fluids (Zhang *et al.*, 2018), there was a significant mixing of basinal brine or sea water at the late stage, which could change the fluid composition and generate the late alteration. Secondly, the textures of dissolution and re-precipitation along a certain direction (probably a crack) could also indicate late fluid alteration. Thus, an external fluid mixing into the former fluid that formed T_{D1}-L magnetite can be considered as the main reason for fluid composition changes, which subsequently generated the T_{D1}-D magnetite. In addition, the compositional variation of granular magnetite (T_{D2}) might be controlled in the main by temperature.

Origins and evolution of Duotoushan magnetite

According to Dare *et al.* (2014), magnetite can be derived from either silicate melts or hydrothermal fluids. The behaviour of Ni

Table 1. Mean, minimum and maximum contents (wt.%) for magnetite from the Duotoushan deposit.

Magnetite type		SiO_2	CaO	NiO	MgO	FeO	Al_2O_3	MnO	Cr_2O_3	V_2O_3	TiO_2
T_{D1}-L (n = 9)	Mean	0.196	0.002	0.010	0.016	92.875	0.042	0.054	0.012	0.002	0.011
	Min	0.113	b.d.l.	b.d.l.	0.010	92.268	0.035	0.036	b.d.l.	b.d.l.	b.d.l.
	Max	0.306	0.010	0.026	0.024	93.433	0.052	0.069	0.021	0.010	0.025
T_{D1}-D (n = 9)	Mean	2.594	0.388	0.001	0.181	89.986	0.189	0.054	0.023	0.005	0.014
	Min	2.267	0.222	b.d.l.	0.011	88.518	0.096	0.044	0.015	b.d.l.	b.d.l.
	Max	3.433	0.648	0.010	0.288	91.011	0.338	0.076	0.032	0.017	0.030
T_{D2}-L (n = 26)	Mean	0.671	0.002	0.002	0.012	92.411	0.064	0.056	0.010	0.007	0.012
	Min	0.158	b.d.l.	b.d.l.	b.d.l.	91.547	b.d.l.	0.027	b.d.l.	b.d.l.	b.d.l.
	Max	1.249	0.025	0.010	0.035	93.314	0.253	0.094	0.032	0.023	0.042
T_{D2}-D (n = 28)	Mean	2.192	0.351	0.004	0.086	89.298	0.526	0.087	0.010	0.009	0.098
	Min	0.984	0.030	b.d.l.	0.018	87.860	0.221	0.049	b.d.l.	b.d.l.	0.010
	Max	3.207	0.644	0.021	0.137	91.358	0.714	0.135	0.044	0.025	0.175

n = Number of analyses; b.d.l. = below detection limit

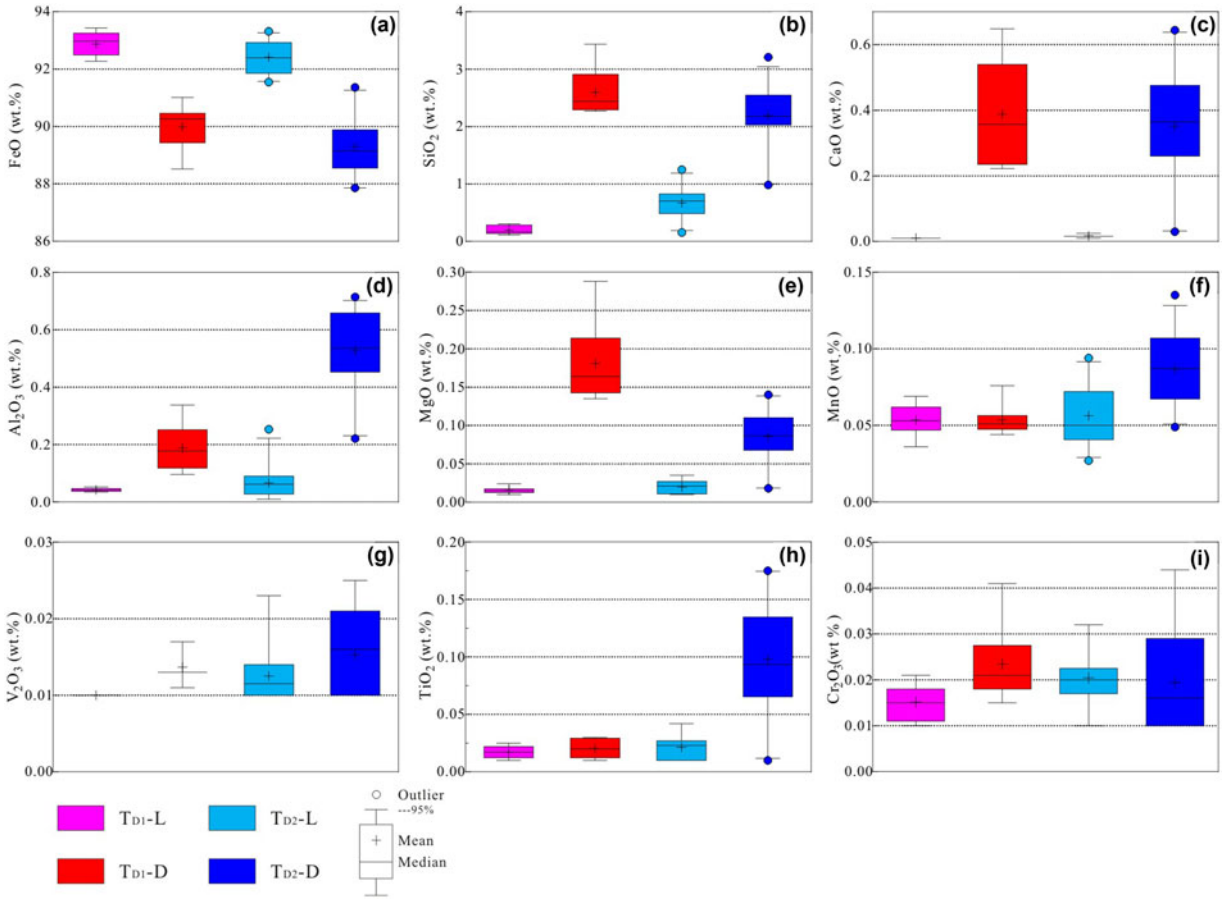

Fig. 7. Box and whisker plots for minor- and trace-element concentrations in magnetite from the Duotoushan deposit. The whiskers represent the minimum and maximum values. The element concentrations below detection limits were excluded from the box and whisker plots.

and Cr in magmatic magnetite is quite different from that in hydrothermal magnetite. Their behaviour is coupled in silicate magmas and the Ni/Cr ratio of magnetite ≤1. In contrast, in many hydrothermal environments (i.e. porphyry, IOCG, skarn), their behaviour is decoupled and the Ni/Cr ratio of magnetite ≥1, and this can probably be attributed to a greater solubility of Ni compared to Cr in fluids. Therefore, a plot of Ti *vs.* Ni/Cr can be used to discriminate magnetite between hydrothermal and magmatic environments (Dare *et al.*, 2014). At the Duotoushan deposit, both types of magnetite are of hydrothermal origin which is characterised by low-Ti and high-Ni/Cr relative to those of magmatic magnetite (Fig. 10). Moreover, magnetite in the Duotoushan deposit commonly co-precipitated with hydrothermal minerals, e.g. amphibole and epidote (Fig. 3), also suggesting a hydrothermal origin.

Most investigations refer to the platy magnetite as mushketovite which formed by replacing primary hematite. The transformation of hematite to magnetite may undergo a redox reaction,

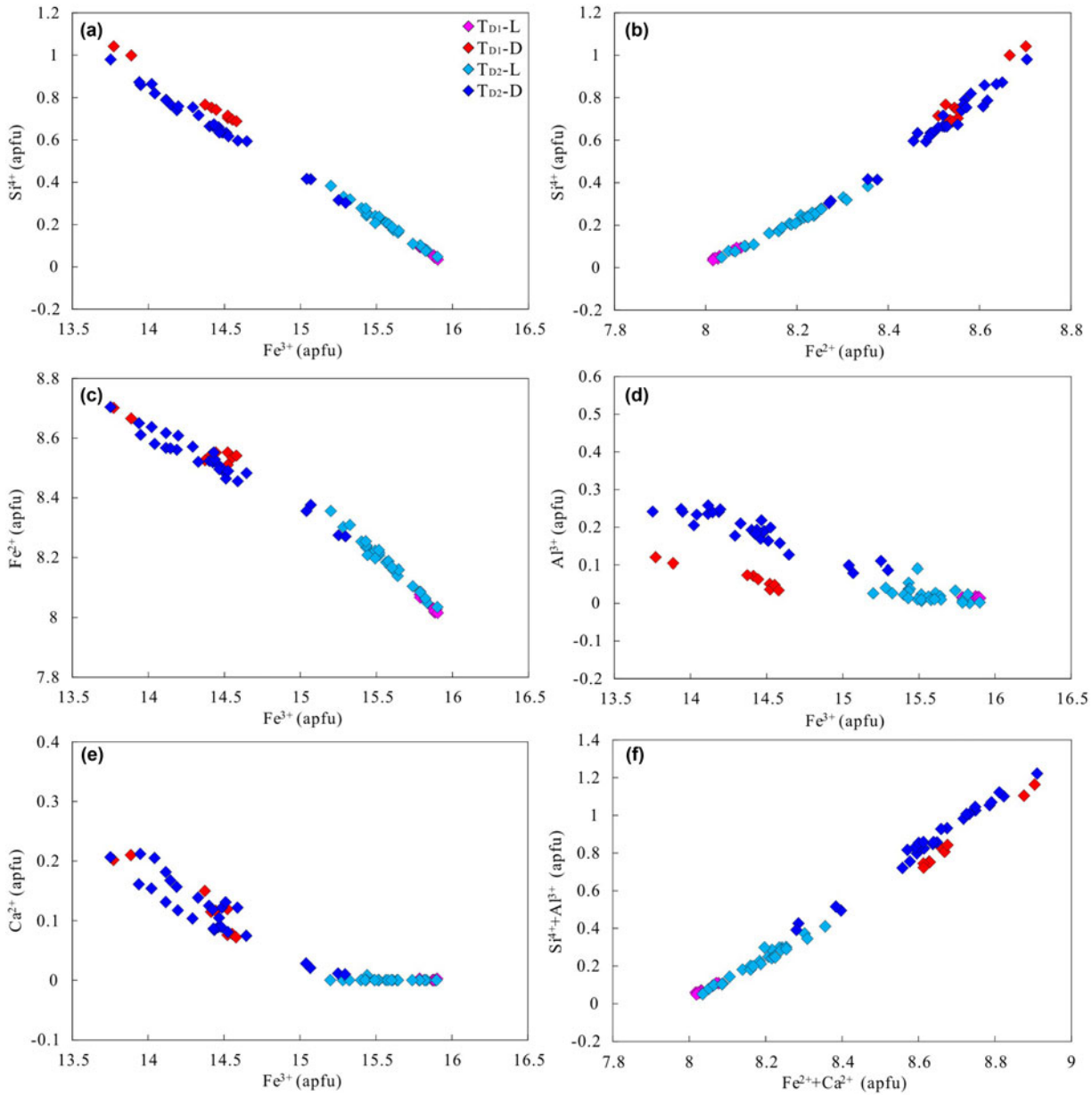

Fig. 8. The binary plots of magnetite composition from the Duotoushan deposit indicating that trace elements were incorporated into magnetite by substitution of divalent, trivalent and/or tetravalent cations for iron: (*a*) Si^{4+} *vs.* Fe^{3+}; (*b*) Si^{4+} *vs.* Fe^{2+}; (*c*) Fe^{2+} *vs.* Fe^{3+}; (*d*) Al^{3+} *vs.* Fe^{3+}; (*e*) Ca^{2+} *vs.* Fe^{3+}; (*f*) $Si^{4+}+Al^{3+}$ *vs.* $Fe^{2+}+Ca^{2+}$.

which results in a volume decrease of 1.64% (Ohmoto, 2003; Mucke and Cabral, 2005). This figure is established by calculation (using *Adobe Photoshop CS4*) that the proportion of pore volume in the whole T_{D1}-L magnetite is ~0.77% (Fig. 11a–c), which is significantly less than the theoretical volume of decrease (1.64%). In general, the pores formed by the transformation of hematite to magnetite are distributed homogeneously. But the abundant pores found in the T_{D1}-D magnetite are distributed very unevenly and usually occur along the edge or cracks of T_{D1}-L magnetite (Fig. 4b). In addition, the calculated proportion of pore volume in the whole T_{D1}-D magnetite is ~4.44% (Fig. 11d–f), much greater than 1.64%, indicating that T_{D1}-D magnetite is not the product of hematite transforming to magnetite, but rather resulted from the later fluids as discussed above. Given the evidence, platy magnetite is more likely to be precipitated from the hydrothermal fluid rather than transformation from primary hematite. Magnetite has a cubic inverse spinel structure and usually forms crystals with octahedral morphology (Fig. 11g). Previous studies have shown that some external environmental conditions, e.g. crystal growth rate, growth space, and stress action, will also have an affect on the crystal morphology (Liu *et al.*, 2006; Li, 2008; Wang *et al.*, 1982). If the growth space along [001] is limited, or the growth rate along [001] is much slower than that along [100] and [010], magnetite might occur as platy crystals rather than octahedrons (Fig. 11h). According to the observation above, T_{D1} magnetite is generally intergrown with platy amphibole (Fig. 3b). Therefore, magnetite might appear as platy crystals due to the limitation of growth space and the growth habit of coexisting minerals (i.e. amphibole).

On the basis of the discussion above, we have speculated about the origins and evolutionary processes of magnetite from the Duotoushan deposit and illustrated them schematically in

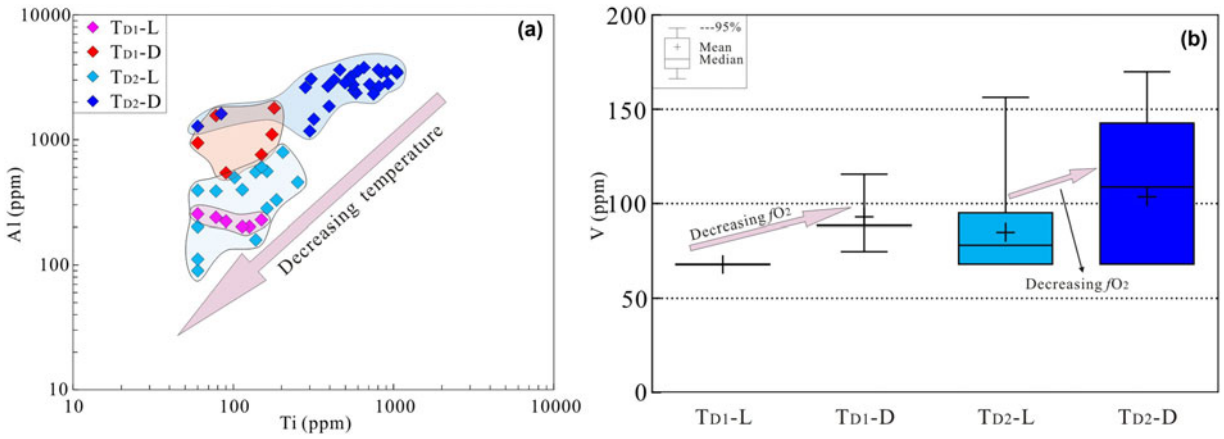

Fig. 9. (*a*) Plot of Al *vs.* Ti for the Duotoushan magnetite. The high-temperature magnetite typically plots in the high-Ti and Al contents fields; (*b*) Plot of V concentration for the Duotoushan magnetite. V^{3+} has the highest compatibility with the spinel structure of magnetite and V^{5+} is incompatible at high oxygen fugacity levels (Balan *et al.*, 2006; Righter *et al.*, 2006). Therefore, a higher V concentration might indicate lower f_{O_2}.

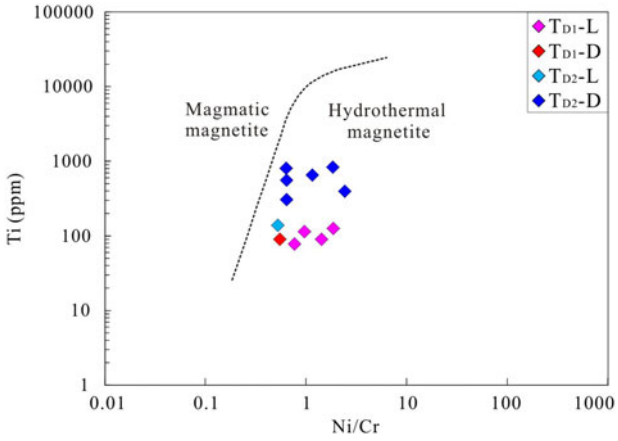

Fig. 10. Discrimination diagram of Ti (ppm) *vs.* Ni/Cr in magnetite from the Duotoushan Fe–Cu deposit. Reference fields from Dare *et al.* (2014).

Fig. 12. Although the possibility that platy magnetite transformed from hematite cannot be excluded entirely (Fig. 12a), we suggest that platy magnetite associated with amphibole was originally precipitated from hydrothermal fluid (Fig. 12b). Subsequently, an external fluid may have mixed with the previous fluid and consequently caused the undersaturation of iron in the fluids, leading to dissolution of primary magnetite (T_{D1}-L; greater Fe and lesser Si, Al, Ca concentrations) and re-precipitation of T_{D1}-D magnetite (less Fe and more Si, Al, Ca) with significant porosity and abundant mineral inclusions (Fig. 12c). We observed that T_{D1}-D magnetite usually formed along fractures of the platy magnetite (Fig. 6a). According to the structure model of granular and platy magnetite (Fig. 11g, h), when there is a force along [001], the platy magnetite is more likely to generate fractures than granular magnetite. Therefore, the later external fluid has a significant effect on T_{D1} but less influence on T_{D2} magnetite. This external fluid might contain basin brine or seawater with high salinity and Cl^- contents and thus enhanced the solubility of Fe, a suggestion which is supported by hydrogen and oxygen isotopic compositions of fluid inclusions (Zhang *et al.*, 2018). By comparison, granular magnetite associated with epidote, quartz and minor amphibole was precipitated from fluid that formed T_{D1}-L magnetite. With periodic variation in temperature, oscillatory zoning (with zones of various widths) was formed in granular magnetite (Fig. 12d) to avoid intensive alteration from late external fluids due to lack of structural weakness. These oscillatory bands are characterised by bands depleted in Si, Al and Ca (T_{D2}-L magnetite) alternating with bands enriched in these elements (T_{D2}-D magnetite).

Implications for genesis of Fe–Cu ore deposits

The origins of magnetite in different types of Fe–Cu deposits are variable. Previous studies have shown that trace elements of magnetite can be used to identify ore-deposit types and genesis of mineral deposits (Dupuis and Beaudoin, 2011; Dare *et al.*, 2014; Nadoll *et al.*, 2014; Chen *et al.*, 2015; Knipping *et al.*, 2015a, b; Heidarian *et al.*, 2016; Huang *et al.*, 2014, 2018). The plot of Ca + Al + Mn *vs.* Ti + V proposed by Dupuis and Beaudoin (2011) is one of the most widely used discrimination diagrams at present. It can be used to differentiate magnetite from a variety of ore-deposit types (i.e. porphyry, Kiruna, IOCG, BIF, skarn and Fe-Ti-V). This discrimination diagram does not work very well for magnetite in a complex hydrothermal deposit such as Duotoushan in the present study.

As shown in Fig. 13, all T_{D1}-D magnetite data fall in the skarn field and most of the T_{D1}-L magnetite data fall below the skarn field, which probably resulted from dissolution and re-precipitation process. This process caused the magnetite with less Ca, Al and Mn to dissolve and then re-precipitate magnetite with more Ca, Al and Mn and significant porosity and abundant mineral inclusions. Similarly, the composition of T_{D2} magnetite shows, in general, a much larger elemental dispersion with most T_{D2}-L magnetite plotting in the fields of BIF and all of T_{D2}-D magnetite plotting in the field of skarn. This elemental dispersion might result from the oscillatory zoning (as T_{D1}-D magnetite is rich in Ca, Al and Ti whereas T_{D2}-L magnetite contains less of these elements), resulting from periodic change in temperature during hydrothermal processes.

In summary, trace-element concentrations in most magnetite from Fe–Cu deposits, such as at Duotoushan, are similar to those observed in hydrothermal systems, such as IOCG and skarn deposits. In addition, although the discrimination diagrams based on magnetite composition do provide a good baseline for

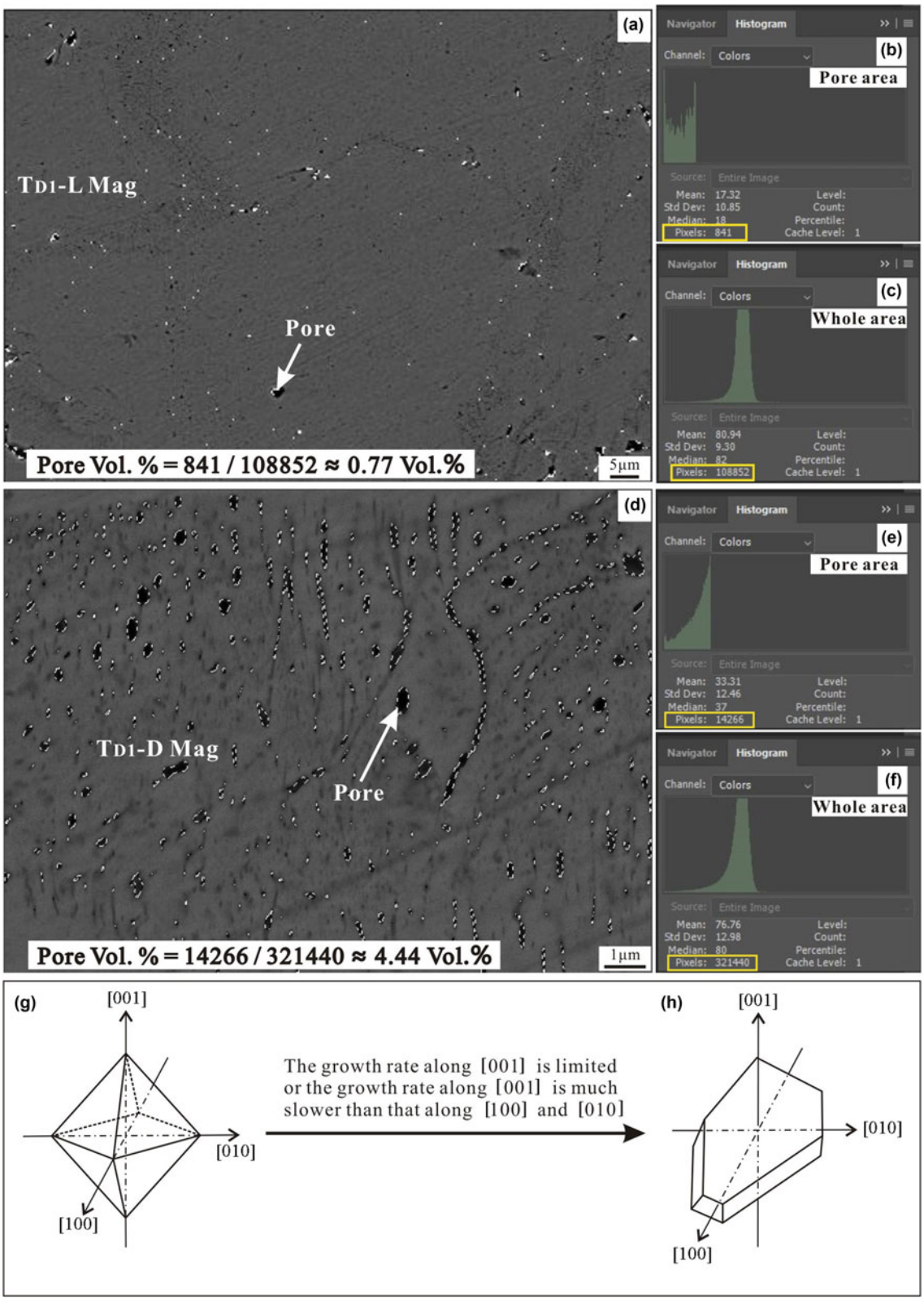

Fig. 11. Estimation of the pore volume (calculated using *Adobe Photoshop* CS4) (*a*–*b*) and the structure model of magnetite (*g*–*h*). The smallest unit of an image is a pixel and thus the area percentage can be represented by the pixel percentage. (*a*) T_{D1}-L magnetite. White dashed circles are the pores identified by the Polygonal Lasso Tool in the software. (*b*–*c*) The pixels representing pore area and the total T_{D1}-L magnetite area calculated by the software, respectively. The ratio of pixels in pore area and whole area, i.e. 0.77%, is the proportion of pore volume in the whole T_{D1}-L magnetite. (*d*) T_{D1}-D magnetite. Similarly, white dashed circles are the pore identified by the Polygonal Lasso Tool in the software. (*e*–*f*) The pixels of the pore area and the whole T_{D1}-D magnetite area calculated by software, respectively. Therefore, the ratio of pixels in pore area and whole area, i.e. 4.44%, is the proportion of pore volume in the whole T_{D1}-D magnetite. (*g*) The structure model of magnetite octahedrons. (*h*) The platy crystal of magnetite. If the growth space along [001] is limited, or the growth rate along [001] is much slower than that along [100] and [010], magnetite may have occurred as platy crystals rather than as octahedrons.

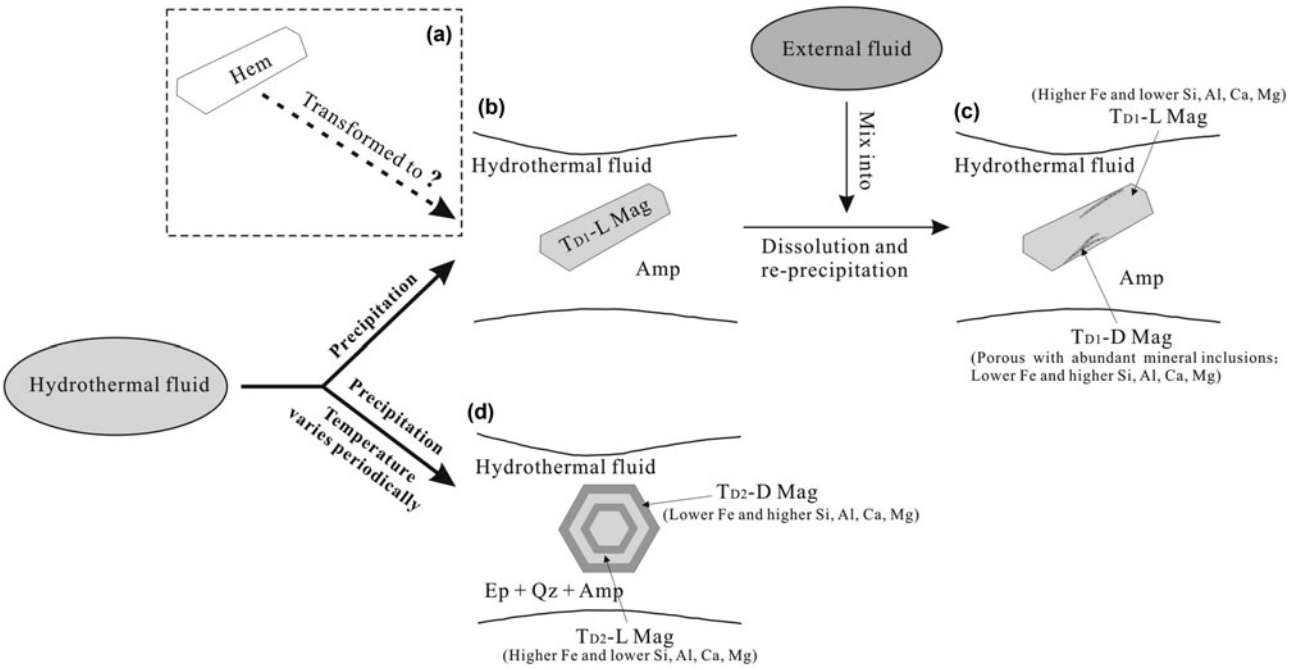

Fig. 12. Sketches illustrating the genesis of magnetite from the Duotoushan deposit. (*a*) Platy magnetite was probably mushketovite transformed from hematite, which we cannot completely rule out from our data. (*b*) Platy magnetite (T_{D1}-L) associated with amphibole (Amp) was more probably originally precipitated from hydrothermal fluid; (*b*) An external fluid mixed into the primary fluid and resulted in the dissolution of T_{D1}-L magnetite and re-precipitation of T_{D1}-D magnetite; (*c*) Granular magnetite associated with epidote (Ep), quartz (Qz) and amphibole was precipitated from the primary fluid. Then, with the periodic temperature changes, T_{D2}-L magnetite was depleted in Si, Al and Ca; and T_{D2}-D magnetite enriched in these elements was formed.

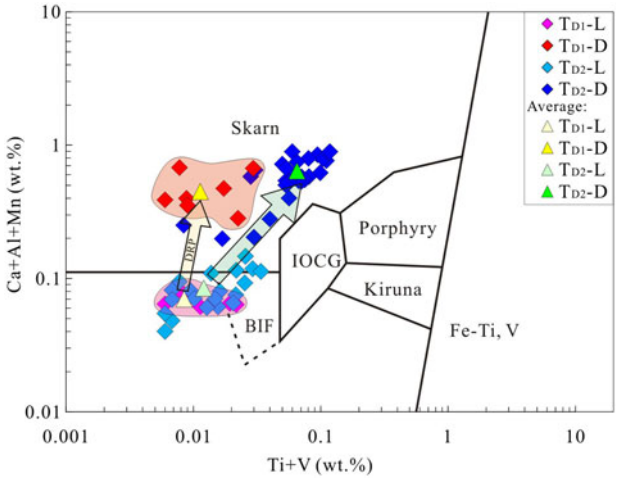

Fig. 13. Plot of Ca + Al + Mn *vs.* Ti + V (wt.%) in magnetite from the Duotoushan Fe–Cu deposit. Reference fields from Dupuis and Beaudoin (2011).

the ore-genesis discrimination of Fe–Cu deposits, detailed textural characterisation prior to compositional analysis is critical.

Conclusions

The Duotoushan Fe–Cu deposit contains two different types of magnetite (platy and granular) based on textural and chemical characteristics. The platy and granular magnetite may have precipitated from hydrothermal fluids under different conditions. Both the platy and granular magnetite display two types of compositional zoning, although their genetic mechanisms are different. According to our data the zoning of platy magnetite was more likely to have been formed by a dissolution–re-precipitation process caused by change in the fluid composition, whereas that of granular magnetite was caused by precipitation of fluids with cyclical changes in temperature. These oscillatory zones are characterised by bands enriched in Si, Al and Ca alternating with bands depleted in these elements. Magnetite in the Duotoushan Fe–Cu deposit have compositions similar to those in the IOCG and skarn deposits and experienced a very complex evolution process. We further suggest that detailed textural characterisation prior to compositional analysis is critical in the study of the ore genesis and evolution of Fe–Cu deposits.

Supplementary material. To view supplementary material for this article, please visit https://doi.org/10.1180/mgm.2020.29

Acknowledgements. This study was funded by the National Natural Science Foundation of China (U1603244), Chinese National Science Fund (41725009) and Type-B Chinese Academy of Sciences Strategic Pilot Science and Technology Special (XDB18030206). In particular, the authors are grateful to Prof. Xiangping Gu (Central South University) and Xi Chen (Southwest Petroleum University) for their help with XRD and EMPA analyses.

References

Alaminia Z., Tadayon M., Finger F., Lentz D.R. and Waitzinger M. (2020) Analysis of the infiltrative metasomatic relationships controlling skarn mineralization at the Abbas-Abad Fe–Cu Deposit, Isfahan, north Zefreh Fault, Central Iran. *Ore Geology Reviews*, 117, https://doi.org/10.1016/j.oregeorev.2020.103321

Apukhtina O.B., Kamenetsky V.S., Ehrig K., Kamenetsky M.B., Maas R., Thompson J., McPhie J., Ciobanu C.L. and Cook N.J. (2017) Early, deep magnetite-fluorapatite mineralization at Olympic Dam Cu-U-Au deposit, South Australia. *Economic Geology*, **112**, 1531–1542.

Balan E., De Villiers J.P.R., Eeckhout S.G., Glatzel P., Toplis M.J. and Fritsch E. (2006) The oxidation state of vanadium in titanomagnetite from layered basic intrusions. *American Mineralogist*, **91**, 953–956.

Canil D., Grondahl C., Lacourse T. and Pisiak L.K. (2016) Trace elements in magnetite from porphyry Cu–Mo–Au deposits in British Columbia, Canada. *Ore Geology Reviews*, **72**, 1116–1128.

Carew M.J. (2004) *Controls on Cu-Au mineralization and Fe oxide metasomatism in the Eastern Fold Belt, N.W. Queensland, Australia*. PhD thesis, James Cook University, Queensland, Australia.

Chen Y.J., Ni P., Fan H.R., Pirajno F., Lai Y., Su W.C. and Zhang H. (2007) Diagnostic fluid inclusions of different types hydrothermal gold deposits. *Acta Petrologia Sinica*, **23**(9), 2085–2108 [in Chinese with English abstract].

Chen Y.J., Zhai M.G. and Jiang S.Y. (2009) Significant achievements and open issues in study of orogenesis and metallogenesis surrounding the North China continent. *Acta Petrologia Sinica*, **25**(11), 2695–2726 [in Chinese with English abstract].

Chen Y.J., Pirajno F., Wu G., Qi J.P. and Xiong X.L. (2012) Epithermal deposits in north Xinjiang, NW China. *International Journal of Earth Science*, **101**, 889–917.

Chen W.T., Zhou M.F., Gao J.F. and Hu R. (2015) Geochemistry of magnetite from Proterozoic Fe–Cu deposits in the Kangdian metallogenic province, SW China. *Mineralium Deposita*, **50**, 795–809.

Ciobanu C.L. and Cook N.J. (2004) Skarn textures and a case study: the Ocna de Fier-Dognecea orefield, Banat, Romania. *Ore Geology Reviews*, **24**, 315–370.

Dare S.A.S., Barnes S.J. and Beaudoin G. (2012) Variation in trace element content of magnetite crystallized from a fractionating sulfide liquid, Sudbury, Canada: Implications for provenance discrimination. *Geochimica et Cosmochimica Acta*, **88**, 27–50.

Dare S.A.S., Barnes S.J., Beaudoin G., Méric J., Boutroy E. and Potvin-Doucet C. (2014) Trace elements in magnetite as petrogenetic indicators. *Mineralium Deposita*, **49**, 785–796.

Dare S.A.S., Barnes S.J. and Beaudoin G. (2015) Did the massive magnetite "lava flows" of El Laco (Chile) form by magmatic or hydrothermal processes? New constraints from magnetite composition by LA-ICP-MS. *Mineralium Deposita*, **50**, 607–617.

Deditius A.P., Reich M., Simon A.C., Suvorova A., Knipping J., Roberts M.P., Rubanov S., Dodd A. and Saunders M. (2018) Nanogeochemistry of hydrothermal magnetite. *Contributions to Mineralogy and Petrology*, **173**, 46, https://doi.org/10.1007/s00410-018-1474-1

Deng X.H., Wang J.B., Wang Y.W., Li Y.C., Fang T.H. and Mao Q.G. (2014) Geological characteristics of the Hongshi Cu–Au deposit, eastern Tianshan, Xinjiang and discussion of the deposit genesis. *Mineral Exploration*, **5**(2), 159–168 [in Chinese with English abstract].

Dupuis C. and Beaudoin G. (2011) Discriminant diagrams for iron oxide trace element fingerprinting of mineral deposit types. *Mineralium Deposita*, **46**, 319–335.

Felipe I.D., Fanlo I., Mateo E. and Subias I. (2014) The Bizielle vein (valle de Gistain): A case of iron oxide transformations at the Pyrenees of Spain. *Chemie der Erde*, **74**, 77–85.

Fukasawa T., Iwatsuki M. and Furukawa M. (1993) State analysis and relationship between lattice constants and compositions including minor elements of synthetic magnetite and maghemite. *Analytica Chimica Acta*, **281**(2), 413–419.

Günther T., Klemd R., Zhang X., Horn I. and Weyer S. (2017) In-situ trace element and Fe-isotope studies on magnetite of the volcanic-hosted Zhibo and Chagangnuoer iron ore deposits in the Western Tianshan, NW China. *Chemical Geology*, **453**, 111–127.

Heidarian H., Lentz D., Alirezaei S., Peighambari S. and Hall D. (2016) Using the chemical analysis of magnetite to constrain various stages in the formation and genesis of the Kiruna-type chadormalu magnetite–apatite deposit, Bafq district, Central Iran. *Mineralogy and Petrology*, **110**, 927–942.

Hou T., Zhang Z.C., Santosh M., Encarnacion J., Zhu J. and Luo W.Q. (2014) Geochronology and geochemistry of submarine volcanic rocks in the Yamansu iron deposit, Eastern Tianshan Mountains, NW China: constraints on the metallogenesis. *Ore Geology Reviews*, **56**, 487–502.

Hu H., Li J.W., Lentz D., Ren Z., Zhao X.F., Deng X.D. and Hall D. (2014) Dissolution–re-precipitation process of magnetite from the Chengchao iron deposit: insights into ore genesis and implication for in-situ chemical analysis of magnetite. *Ore Geology Reviews*, **57**, 393–405.

Hu H., Lentz D., Li J.W., McCarron T., Zhao X.F. and Hall D. (2015) Reequilibration processes in magnetite from iron skarn deposits. *Economic Geology*, **110**(1), 1–8.

Hu X., Chen H.Y., Zhao L.D., Han J.S. and Xia X.P. (2017) Magnetite geochemistry of the Longqiao and Tieshan Fe-(Cu) deposits in the Middle-Lower Yangtze River Belt: Implications for deposit type and ore genesis. *Ore Geology Reviews*, **89**, 823–835.

Hu X., Chen H.Y., Beaudoin G. and Zhang Y. (2020) Textural and compositional evolution of iron oxides at Mina Justa (Peru): Implications for mushketovite and formation of IOCG deposits. *American Mineralogist*, **105**, 397–408.

Huang X.W., Qi L., Gao J.F. and Zhou M.F. (2013) First reliable Re-Os ages of pyrite and stable isotope compositions of Fe (-Cu) deposits in the Hami Region, Eastern Tianshan Orogenic Belt, NW China. *Resource Geology*, **63**, 166–187.

Huang X.W., Qi L. and Meng Y.M. (2014) Trace element geochemistry of magnetite from the Fe (-Cu) deposits in the Hami Region, Eastern Tianshan Orogenic Belt, NW China. *Acta Geologica Sinica*, **88**(1), 176–195.

Huang X.W., Zhou M.F., Qiu Y.Z., Qi L. (2015a) In-situ LA-ICP-MS trace elemental analyses of magnetite: The Bayan Obo Fe-*REE*-Nb deposit, North China. *Ore Geology Reviews*, **65**, 884–899.

Huang X.W., Gao J.F., Qi L., Zhou M.F. (2015b) In-situ LA-ICP-MS trace elemental analyses of magnetite and Re-Os dating of pyrite: The Tianhu hydrothermally remobilized sedimentary Fe deposit, NW China. *Ore Geology Reviews*, **65**, 900–916.

Huang X.W., Gao J.F., Qi L., Meng Y.M., Wang Y.C. and Dai Z.H. (2016) In-situ LA-ICP-MS trace elements analysis of magnetite: The Fenghuangshan Cu-Fe-Au deposit, Tongling, Eastern China. *Ore Geology Reviews*, **72**, 746–759.

Huang X.W., Zhou M.F., Beaudoin G., Gao J.F., Qi L. and Lyu C. (2018) Origin of the volcanic-hosted Yamansu Fe deposit, eastern Tianshan, NW China: constraints from pyrite Re-Os isotopes, stable isotopes, and in situ magnetite trace elements. *Mineralium Deposita*, **53**, 1039–1060.

Huang X.W. and Beaudoin G. (2019) Textures and chemical compositions of magnetite from iron oxide copper-gold (IOCG) and kiruna-type iron oxide-apatite (IOA) deposits and their implications for ore genesis and magnetite classification schemes. *Economic Geology*, **114**(5), 953–979. http://hdl.handle.net/20.500.11794/34394

Jia G.Z. and Zhao D.H. (2017) Geological characteristics and genetic model of the Duotoushan iron deposit, Xinjiang, China. *Xinjiang Non-Ferrous Metals*, **3**, 48–51 [in Chinese].

Knipping J.L., Bilenker L.D., Simon A.C., Reich M., Barra F., Deditius A.P., Lundstrom C., Bindeman I. and Munizaga R. (2015a) Giant Kiruna-type deposits form by efficient flotation of magmatic magnetite suspensions. *Geology*, **43**, 591–594.

Knipping J.L., Bilenker L.D., Simon A.C., Reich M., Barra F., Deditius A.P., Wälle M., Heinrich C.A., Holtz F. and Munizaga R. (2015b) Trace elements in magnetite from massive iron oxide-apatite deposits indicate a combined formation by igneous and magmatic-hydrothermal processes. *Geochimica et Cosmochimica Acta*, **171**, 15–38.

Li S.R. (2008) *Crystallography and Mineralogy*. Higher Education Press, Beijing, pp. 14–15.

Lindsley D.H. (1976) The crystal chemistry and structure of oxide minerals as exemplified by the Fe–Ti oxides. Pp. L1–L60 in: *Oxide Minerals* (D. Rumble III, editor). Reviews in Mineralogy. Mineralogical Society of America, Chantilly, Virginia, USA.

Liu X.M., Fu S.Y. and Xiao H.M. (2006) Fabrication of octahedral magnetite microcrystals. *Materials Letters*, **60**, 2979–2983.

Makvandi S., Beaudoin G., McClenaghan B.M. and Layton-Matthews D. (2015) The surface texture and morphology of magnetite from the Izok Lake volcanogenic massive sulfide deposit and local glacial sediments, Nunavut, Canada: application to mineral exploration. *Journal of Geochemical Exploration*, **150**, 84–103.

Makvandi S., Ghasemzadeh-Barvarz M., Beaudoin G., Grunsky E.C., McClenaghan M.B. and Duchesne C. (2016) Principal component analysis

of magnetite composition from volcanogenic massive sulfide deposits: Case studies from the Izok Lake (Nunavut, Canada) and Halfmile Lake (New Brunswick, Canada) deposits. *Ore Geology Reviews*, **72**, 60–85.

McIntire W.L. (1963) Trace element partition coefficients—a review of theory and applications to geology. *Geochimica et Cosmochimica Acta*, **27**, 1209–1264.

Mucke A. and Cabral A.R. (2005) Redox and nonredox reactions of magnetite and hematite in rocks. *Chemie der Erde*, **65**, 271–278.

Nadoll P., Mauk J.L., Hayes T.S., Koenig A.E. and Box S.E. (2012) Geochemistry of magnetite from hydrothermal ore deposits and host rocks of the Mesoproterozoic Belt Supergroup, United States. *Economic Geology*, **107**, 1275–1292.

Nadoll P., Angerer T., Mauk J.L., French D. and Walshe J. (2014) The chemistry of hydrothermal magnetite: A review. *Ore Geology Reviews*, **61**, 1–32.

Newberry N.G., Peacor D.R., Essene E.J. and Geissman J.W. (1982) Silicon in magnetite: High resolution microanalysis of magnetite-ilmenite intergrowths. *Contributions to Mineralogy and Petrology*, **80**, 334–340.

Nielsen R.L., Forsythe L.M., Gallahan W.E. and Fisk M.R. (1994) Major- and trace-element magnetite–melt equilibria. *Chemical Geology*, **117**, 167–191.

Ohmoto H. (2003) Nonredox transformations of magnetite–hematite in hydrothermal systems. *Economic Geology*, **98**, 157–161.

Putnis A. (2009) Mineral replacement reactions. Pp. 87–124 in: *Thermodynamics and Kinetics of Water-Rock Interaction* (E. Oelkers and J. Schott, editors). Reviews in Mineralogy & Geochemistry, **70**, Mineralogical Society of America, Chantilly, Virginia, USA.

Putnis A. and John T. (2010) Replacement processes in the Earth's crust. *Elements*, **6**, 159–164.

Righter K., Leeman W.P. and Hervig R.L. (2006) Partitioning of Ni, Co and V between spinel-structured oxides and silicate melts: importance of spinel composition. *Chemical Geology*, **227**, 1–25.

Rusk B., Oliver N., Brown A., Lilly R. and Jungmann D. (2009) Barren magnetite breccias in the Cloncurry region, Australia: comparisons to IOCG deposits. *Society for Geology Applied to Ore Deposits 10th Biennial Meeting, Townsville, Australia*, pp. 656–658.

Sang S.J., Peng M.X. and Guo Y.H. (2003) Optimized Target Areas and Evaluation Report of Resource in the Caixiashan to Jintan Area. *Xingjiang Institute of Geological Investigation*, pp. 42–44 [in Chinese]. docin.com/p-81748606.html.

Sengör A.M.C., Natal'In B.A. and Burtman V.S. (1993) Evolution of the Altaid tectonic collage and Paleozoic crustal growth in Eurasia. *Nature*, **364**, 299–307.

Sengör A.M.C. and Natal'in B.A. (1996) Paleotectonics of Asia: fragments of synthesis. Pp. 486–640 in: *The Tectonic Evolution of Asia* (A. Yin and T.M. Harrison, editors). Cambridge University Press, Cambridge, UK.

Shannon R.D. (1976) Revised effective ionic radii and systematic study of inter atomic distances in halides and chalcogenides. *Acta Crystallographica*, **A32**, 751–767.

Shimazaki H. (1998) On the occurrence of Silician magnetites. *Resource Geology*, **48**, 23–29 https://doi.org/10.1111/j.1751-3928.1998.tb00004.x

Singoyi B., Danyushevsky L., Davidson G.J., Large R. and Zaw K. (2006) Determination of trace elements in magnetites from hydrothermal deposits using the LA-ICP-MS technique. *Abstracts of Oral and Poster Presentations from the SEG 2006 Conference Society of Economic Geologist*, Keystone, USA, pp. 367–368.

Wang L.S., Li H.Q., Chen Y.C. and Liu D.Q. (2005) Geological feature and mineralization epoch of Bailingshan iron deposit, Hami, Xingjiang, China. *Mineral Deposits*, 24(3), 280–284 [in Chinese with English abstract].

Wang J.B., Wang Y.W. and He Z.J. (2006) Ore deposits as a guide to the tectonic evolution in the East Tianshan Mountains, NW China. *Geology in China*, 33(3), 461–469 [in Chinese with English abstract].

Wang P., Pan Z.L. and Weng L.B. (1982) *Systematic Mineralogy*. Geology Publishing House, Beijing, pp. 84–90.

Wechsler B.A., Lindsley D.H. and Prewitt C.T. (1984) Crystal structure and cation distribution in titanomagnetites ($Fe_{3-x}Ti_xO_4$). *American Mineralogist*, **69**, 754–770.

Wen G., Li J.W., Hofstra A.H., Koenig A.E., Lowers H.A. and Adams D. (2017) Hydrothermal reequilibration of igneous magnetite in altered granitic plutons and its implications for magnetite classification schemes: Insights from the Handan-Xingtai iron district, North China Craton. *Geochimica et Cosmochimica Acta*, **213**, 255–270.

Westendorp R.W., Watkinson D.H. and Jonasson I.R. (1991) Silicon-bearing zoned magnetite crystals and the evolution of hydrothermal fluids at the Ansil Cu-Zn mine, Rouyn-Noranda, Quebec. *Economic Geology*, **86**, 1110–1114.

Whitney D.W. and Evans B.L. (2010) Abbreviations for names of rock-forming minerals. *American Mineralogist*, **95**, 185–187.

Windley B.F., Allen M.B., Zhang C., Zhao Z.Y. and Wang G.R. (1990) Paleozoic accretion and Cenozoic redeformation of the Chinese Tien Shan range, central Asia. *Geology*, **18**, 128–131.

Xiao W.J., Huang B.C., Han C.M., Sun S. and Li J.L. (2010) A review of the western part of the Altaids: a key to understanding the architecture of accretionary orogens. *Gondwana Research*, **18**, 253–273.

Xu H., Shen Z. and Konishi H. (2014) Si-magnetite nano-precipitates in silician magnetite from banded iron formation: Z-contrast imaging and ab initio study. *American Mineralogist*, **99**, 2196–2202.

Yin S., Ma C.Q. and Robinson P.T. (2017) Textures and high field strength elements in hydrothermal magnetite from a skarn system: Implications for coupled dissolution-reprecipitation reactions. *American Mineralogist*, **102**, 1045–1056.

Zhang Z.J., Sun J.B., Hu Y.M., Ji H.W. and Chen W. (2012) Study on stable isotopic characteristics of the Hongyuntan iron deposit of Eastern Tianshan and their implications for the process of mineralization. *Acta Geoscientica Sinica*, 33(6), 918–924 [in Chinese with English abstract].

Zhang W.F., Chen H.Y., Peng L.H., Zhao L.D., Lu W.J., Zhang Z.J., Yang J.T. and Sun J. (2018) Ore genesis of the Duotoushan Fe–Cu deposit, Eastern Tianshan, NW China: Constraints from ore geology, mineral geochemistry fluid inclusion and stable isotopes. *Ore Geology Reviews*, **100**, 401–421.

Zhao W.W. and Zhou M.F. (2015) In-situ LA-ICP-MS trace elemental analyses of magnetite: The Mesozoic Tengtie skarn Fe deposit in the Nanling Range, South China. *Ore Geology Reviews*, **65**, 872–883.